

MERGING GALAXIES WITH TIDAL TAILS IN COSMOS TO $z = 1$ ZHANG ZHENG WEN (闻璋正)^{1,2} AND XIAN ZHONG ZHENG (郑宪忠)¹*Draft version March 5, 2024*

ABSTRACT

Tidal tails are created in major mergers involving disk galaxies. How the tidal tails trace the assembly history of massive galaxies remains to be explored. We identify a sample of 461 merging galaxies with long tidal tails from 35 076 galaxies mass-complete at $M_* \geq 10^{9.5} M_\odot$ and $0.2 \leq z \leq 1$ based on *HST*/ACS F814W imaging data and public catalogs of the COSMOS field. The long tails refer to these with length equal to or longer than the diameter of their host galaxies. The mergers with tidal tails are selected using our novel $A_0 - D_0$ technique for strong asymmetric features together with visual examination. Our results show that the fraction of tidal-tailed mergers evolves mildly with redshift, as $\sim (1+z)^{2.0 \pm 0.4}$, and becomes relatively higher in less massive galaxies out to $z = 1$. With a timescale of 0.5 Gyr for the tidal-tailed mergers, we obtain that the occurrence rate of such mergers follows $0.01 \pm 0.007 (1+z)^{2.3 \pm 1.4} \text{ Gyr}^{-1}$ and corresponds to ~ 0.3 events since $z = 1$ and roughly one-third of the total budget of major mergers from the literature. For disk-involved major mergers, nearly half of them have undergone a phase with long tidal tails.

Subject headings: galaxies: active — galaxies: evolution — galaxies: interactions — galaxies: structure — techniques: image processing

1. INTRODUCTION

The stellar mass growth of galaxies is driven by in-situ star formation and mergers. Quantifying the relative roles of the two processes across cosmic time is one central task in extragalactic astronomy, and provides key observational constraints on theoretical models of galaxy formation and evolution. The in-situ star formation on galactic scales has been much explored out to high redshift in either the volume-averaged or the sub-population statistic manner. The cosmic star formation rate (SFR) density peaks at $z \sim 2-3$ and declines rapidly since then (Lilly et al. 1996; Madau et al. 1996; Shapley 2011; Madau & Dickinson 2014). The majority of star formation takes place in the main-sequence galaxies which form a tight correlation between SFR and stellar mass (e.g., Schreiber et al. 2015), and mostly hosted by those in the mass regime around M^* (Zheng et al. 2007; Karim et al. 2011). The main sequence relation exists among star-forming galaxies (SFGs) out to high z (e.g., Speagle et al. 2014), and its slope and dispersion are shaped by physical processes related to bulge growth (Guo et al. 2015; Whitaker et al. 2015). The decline of the global SFR density is coupled with the rapid increase of stellar mass density of quiescent galaxies since $z \sim 3$ (Ilbert et al. 2013; Tomczak et al. 2014) continuously fed by SFGs through quenching star formation (e.g., Bell et al. 2007; Faber et al. 2007; Moustakas et al. 2013; Dekel & Burkert 2014; Brennan et al. 2015). In contrast, galaxy merging is not only an important process regulating the assembly of galaxies, but also a key mechanism in triggering starburst, shaping galaxy structure, igniting active galactic nucleus (AGN), and ceasing further star formation through exhausting gas or AGN/supernova feedback (e.g., Mihos & Hernquist 1996; Di Matteo et al. 2005; Springel et al. 2005a,b; Croton et al. 2006; Hopkins et al. 2006, 2008).

Galaxy merger rate as a function of redshift is one of funda-

mental relationships to delineate the hierarchical growth history of galaxies and cosmic structures (e.g., White & Rees 1978; Somerville et al. 2008). On the theoretical side, N -body simulations predict that merger rate of dark matter halos strongly evolves with redshift as $(1+z)^m$ and $m = 2 \sim 3$ (Gottlöber et al. 2001; Fakhouri & Ma 2008; Genel et al. 2009; Fakhouri et al. 2010), with an uncertainty about a factor of 2 (Hopkins et al. 2010). Conversion of the halo merger rate into galaxy merger rate has to rely on assumptions of baryonic physics adopted in the theoretical models of galaxy evolution such as the sub-halo structures and mass functions, halo occupation statistics, gas hydrodynamics and cooling, star formation and feedback (Jogee et al. 2009; Hopkins et al. 2010 for reference therein). On the observational side, measurements of galaxy merger rate from morphological studies and pair studies are not consistent with each other (Lotz et al. 2011). The discrepancy arises from uncertainties in sample selection, identification of mergers, correction for false mergers, incompleteness with redshift, cosmic variance and uncertainty in estimation of merger timescale.

Galaxy merger rate is estimated through counting either close pairs (e.g., Kartaltepe et al. 2007; Lin et al. 2008; Bluck et al. 2009; de Ravel et al. 2009; Bundy et al. 2009; Williams et al. 2011; Bluck et al. 2012; Man et al. 2012; Newman et al. 2012; Xu et al. 2012; Keenan et al. 2014; López-Sanjuan et al. 2015) or morphology-disturbed galaxies. For the latter, visual examination and non-parametric methods are widely used to select galaxy major mergers, which often exhibit tidal features like shells, arcs, plumes, rings, streams, tails and double cores. Such disturbed features can be caught in visual inspection (e.g., Jogee et al. 2009; Bridge et al. 2010, hereafter B10). The non-parametric measurements are to quantify morphological parameters, including the rotational asymmetry A (Conselice 2003), Gini- M_{20} (Lotz et al. 2004) or $A_0 - D_0$ (Wen et al. 2014), and separate mergers from those with regular morphologies in the corresponding parametric space. However, morphology studies largely depend on the quality of imaging data as cosmic dimming effect may cause redshift-dependent biases. Noise contamination strongly affects the

¹ Purple Mountain Observatory, Chinese Academy of Sciences, 2 West Beijing Road, Nanjing, 210008, China; zzwen@pmo.ac.cn, xz-zheng@pmo.ac.cn

² University of Chinese Academy of Sciences, 19A Yuquan Road Beijing, China

selection of mergers (Conselice 2003; Conselice et al. 2008, 2009; López-Sanjuan et al. 2009; Shi et al. 2009). Similarly, the Gini coefficient is also influenced by the adopted aperture for a galaxy (Lisker 2008). Another uncertainty in estimating merger rate is related to detection timescale. The averaged timescale for detection of asymmetric features (A) is strongly correlated with the gas fraction and mass ratio of the merger progenitors (Lotz et al. 2008a, 2010a,b, 2011). The contamination of false mergers with peculiar morphologies (Förster Schreiber et al. 2009, 2011) may also account for a significant fraction of the merger candidates preliminarily selected by the non-parameter methods (e.g., Hoyos et al. 2012).

One way to improve the measurements of merger rate is to narrow the selection of galaxy mergers down to a specific type or merging stage so that the related uncertainties can be accordingly reduced (e.g., Lackner et al. 2014). Tidal tails are created in major mergers involving at least one disk galaxy and can be used as a secure sign of major merger event (Toomre & Toomre 1972). Moreover, the tidal tails contain stars and gas, allowing dwarf galaxies and star clusters to form, and contributing to the intergalactic medium (see Duc & Renaud 2013, and references therein). The length and orientation of tidal tails turn out to be regulated by the inclination of progenitor disk galaxies to the approaching orbit. Tidal tails thus trace the assembly history of galaxies with disk progenitors and reflect the alignment of progenitor galaxies in the cosmic web (Yang et al. 2006; Zhang et al. 2009, 2013).

Yet, few works made use of tidal tails as the probe for major mergers to measure merger rate (B10). Tidal tails are faint structures and usually contribute only limited fraction of the total light of a merging system. The morphological parameters rotational asymmetry A , Gini and M_{20} are likely insensitive to probe of such faint structures in a galaxy because these parameters are flux weighted and usually dominated by luminous structures of the galaxy. Wen et al. (2014) developed a novel $A_0 - D_0$ method to select disturbed morphologies through quantifying the outer asymmetry (A_0) and the deviation of the intensity weighted centroids of the outer half light region and the inner half light region (D_0) of a galaxy. This technique is efficient in detecting tidal-tailed galaxies (see Wen et al. 2014 for more details). Galaxies of different morphological types fall on a tight sequence in the A_0 versus D_0 diagram and the tailed galaxies usually have larger A_0 and D_0 relative to those with regular morphologies.

We carry out a search for merging galaxies with long tidal tails in the COSMOS field. The *HST*/ACS F814W (I) imaging observations of the COSMOS survey (Scoville et al. 2007; Koekemoer et al. 2007) cover $\sim 1.5 \text{ deg}^2$ sky area, providing high-resolution images to probe faint structures such as tidal tails (in a size of tens kpc) for a large sample of distant galaxies at $z \leq 1$. This paper is arranged as following: a brief description of the data and sample selection is presented in Section 2; the $A_0 - D_0$ method is given in Section 3. Meanwhile, we perform simulations to test A_0 and D_0 with surface brightness dimming included. In Section 4, we present the selected merging galaxies with tidal tails using the $A_0 - D_0$ method. Finally, we report our merger fraction and merger rate over $0.2 \leq z \leq 1$ in Section 5. Throughout this paper, we adopt a concordance cosmology with $H_0 = 70 \text{ km s}^{-1} \text{ Mpc}^{-1}$, $\Omega_m = 0.3$ and $\Omega_\Lambda = 0.7$. All photometric magnitudes are given in the AB system.

2. DATA AND SAMPLE SELECTION

2.1. The Data

Our study utilizes the public data and catalogs from multi-band deep surveys of the COSMOS field. The UltraVISTA survey (McCracken et al. 2012) provides ultra-deep near-IR imaging observations of this field in the Y , J , H and K_s -band as well as a narrow band (NB118) (Milvang-Jensen et al. 2013). The UltraVISTA photometric catalogs (v4.1) are available to the public, giving in total 154 803 sources based on K_s -band detection down to $5\sigma = 23.4 \text{ mag}$ with 90% completeness for point sources (see Muzzin et al. 2013 for more details). The PSF-matched photometry with 30 photometric bands from 0.15 to $24 \mu\text{m}$, stellar mass and redshift catalogs are also provided. Stellar masses are determined using the FAST SED fitting code (Kriek et al. 2009) while photometric redshifts are derived with the EAZY code (Brammer et al. 2008). Spectroscopic redshifts from the zCOSMOS 10k bright sample (Lilly et al. 2009) are also adopted. The photometric redshifts reach an accuracy of $\delta z/(1+z) = 0.013$ for $z \lesssim 1.5$. Spectroscopic redshifts are first used if available.

The *HST*/ACS I -band imaging data are publicly available, allowing us to measure morphologies in the rest-frame optical for galaxies at $z \leq 1$. The *HST*/ACS I -band images reach a 5σ depth of 27.2 magnitude for point sources. The reduced images have a pixel scale of $0''.03$ and a point spread function (PSF) of Full Width at Half Maximum $0''.09$, corresponding to a physical size of 332 pc at $z = 0.2$ and 805 pc at $z = 1$. Following the source detection configurations given in Leauthaud et al. (2007) and Caldwell et al. (2008), we run the software tool SExtractor (Bertin & Arnouts 1996) to obtain segmentation maps for detected sources. The photometric catalogs of the *HST*/ACS I -band images are also used for source deblending. The segmentation maps will be used to perform morphological analysis. We set the detection threshold to be 0.8σ of background noise level in order to detect extended faint tidal structures (see Wen et al. 2014 for more details).

2.2. Sample Selection

We intend to identify merging galaxies with long tidal tails from a sufficiently large sample of galaxies out to high z . The parent galaxy sample needs to be complete in stellar mass because galaxy mergers often trigger starbursts and increase extinction via condensing interstellar medium (Gavazzi et al. 1996; de Jong 1996; Bell & de Jong 2001; Bell et al. 2003; Kirby et al. 2008). The UltraVISTA catalog based on K_s -band selection is less affected by dust extinction and starburst, and thus shows a higher completeness for low-mass galaxies compared to the optical selection. It has been shown that the UltraVISTA catalog is highly complete (completeness $> 95\%$) for galaxies with stellar mass $\log(M_*/M_\odot) \geq 9.5$ at $z \leq 1$ (Muzzin et al. 2013). We limit sample galaxies at $0.2 \leq z \leq 1$ where *HST* I -band images allow to examine galaxy morphologies in the rest-frame optical. Finally, we select a sample of 35 076 galaxies with $\log(M_*/M_\odot) \geq 9.5$ and $0.2 \leq z \leq 1$ from the UltraVISTA catalog of COSMOS. We measure morphological parameters A_0 and D_0 from *HST* images and visually examine the selected merging galaxies for apparent tidal tails. The parent sample is divided into four mass bins and four redshift bins to address the relationships of the merger rate with stellar mass and redshift (e.g., Lin et al. 2004; Bundy et al. 2005; de Ravel et al. 2009; B10).

3. THE $A_0 - D_0$ SELECTION FOR MERGING GALAXIES

We utilize the $A_O - D_O$ method by Wen et al. (2014) to select galaxies with asymmetric features in galaxy outskirts, including tidal tails. Here we revisit the parameter A_O with an improved noise correction. Simulations are performed to examine how the cosmic dimming effect influences the selection of merging galaxies using the A_O and D_O parameters.

3.1. Morphological Parameters A_O and D_O

The two structural parameters A_O and D_O presented in Wen et al. (2014) give quantitative measures of galaxy structures in the outskirts. The outskirts of a galaxy refers to the outer half-light region (OHR) divided by an elliptical aperture from the inner half-light region (IHR) of the galaxy. The outer asymmetry A_O measures the asymmetry of the OHR; and the outer centroid deviation D_O , measures the deviation (or offset) between the flux-weighted centroids of the IHR and the OHR.

In practice, the half-light aperture is derived from the isophotal analysis of a galaxy image. The surface brightness profile is counted down to the threshold of 0.8σ background rms in order to optimize the detection of faint structures in the outskirts (Wen et al. 2014). We realize that the noise in the low-surface brightness regions bias the estimate of A_O . We thus correct for the bias and revise the definition of A_O as below:

$$A_O = \frac{\sum |I_0 - I_{180}| - \delta_2}{\sum |I_0| - \delta_1}, \quad (1)$$

where $\delta_1 = f_1 * \sum |B_0|$, $f_1 = N_{flux < 1\sigma} / N_{all}$, $\delta_2 = f_2 * \sum |B_0 - B_{180}|$, and $f_2 = N_{|flux| < \sqrt{2}\sigma} / N'_{all}$. Here I_0 refers to the light distribution of the OHR of a galaxy image and I_{180} represents the 180° -rotated version of I_0 . Likewise, B_0 is a patch in the background of the image with the same shape as I_0 . Similarly, B_{180} is the 180° -rotated B_0 . δ_1 and δ_2 are corrections for the noise contributions to the flux image I_0 and the residual image $I_0 - I_{180}$, respectively. f_1 is the number fraction of pixels in the OHR dominated by noise; and f_2 is the number fraction of the OHR pixels dominated by noise in the residual image. N_{all} represents the total number of pixels in the OHR and N'_{all} is the total number of pixels of the residual. Parameter σ is the standard deviation of noise in I_0 . In Wen et al. (2014), the centroid of the OHR is used as the rotational center. But in this work the centroid of the whole galaxy is adopted as the rotational center. More technical details and testing results can be found in the Appendix.

The outer centroid deviation D_O is calculated using the equation

$$D_O = \frac{\sqrt{(x_O - x_I)^2 + (y_O - y_I)^2}}{R_e}, \quad (2)$$

where (x_I, y_I) and (x_O, y_O) refer to the positions of flux-weighted centroids of the IHR and the OHR in a galaxy image, respectively. The deviation is normalized to the effective radius of the galaxy R_e , which is calculated using $R_e = \sqrt{n_I / \pi}$ and n_I is the area of the IHR in units of pixel count. No noise correction is introduced to D_O because background noise does not significantly modify the position of centroid of a galaxy as well as the effective radius.

Galaxies of different morphologies lie on a tight sequence in the $A_O - D_O$ diagram and those exhibiting a higher degree of disturbance in morphology have statistically higher A_O and D_O . The merging galaxies with long tidal tails show high A_O and D_O . The $A_O - D_O$ method has been proved to be effective in selecting tailed galaxies, compared with CAS or Gini- M_{20} selection techniques (Wen et al. 2014).

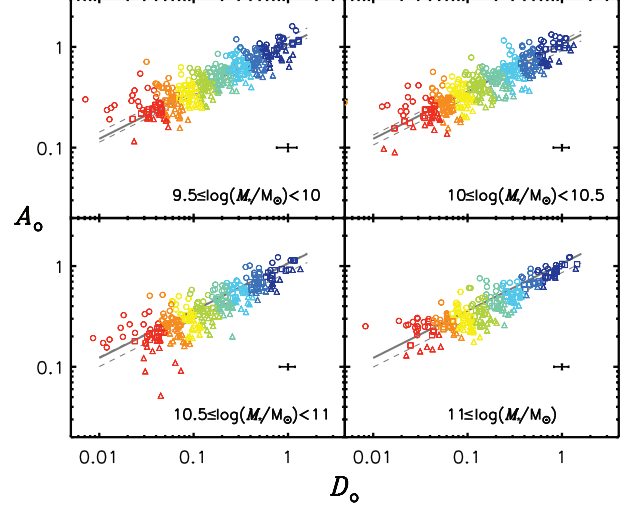


FIG. 1.— Diagram of A_O versus D_O for 1178 galaxies at $0.2 \leq z < 0.4$ from COSMOS. These galaxies form a sequence best-fitted by the solid line. Color coding denotes the 8 bins along the sequence and symbols marks 3 bins vertical to the sequence separated by the dashed lines. The typical 1σ uncertainty in the measurements is marked in each panel.

3.2. Application to High- z Galaxies

We aim to select merging galaxies out to $z = 1$ using the $A_O - D_O$ technique. High- z galaxies appear to be faint and less resolved compared to low- z galaxies. We try to quantitatively estimate these effects on detection of asymmetric structures in galaxy outskirts by measuring the two structural parameters A_O and D_O for a sample of low- z galaxies artificially redshifted to high z . We make use of the 4419 galaxies with $M_* \geq 10^{9.5} M_\odot$ in the lowest redshift bin $0.2 \leq z < 0.4$ to carry out our test. As shown in Figure 1, these galaxies are sub-grouped into 24 bins in the $A_O - D_O$ space: 8 evenly-split bins along the sequence coded by different colors and 3 bins vertical to the sequence marked by different symbols. Objects are divided equally into the three bins vertical to the sequence. We then randomly select 15 galaxies in each bin, yielding 1178 at $0.2 \leq z < 0.4$ with $M_* \geq 10^{9.5} M_\odot$ for further simulations. This sample is representatively spread in the $A_O - D_O$ space and thus able to trace the systematic effects when the sample galaxies are artificially redshifted to high z with resolution and dimming effects counted. This galaxy sample is only used for testing measurements of structural parameters and thus unnecessary to be strictly complete in terms of selections for high- z galaxies.

We use *HST*/ACS *I*-band science images of the selected 1178 galaxies with $M_* \geq 10^{9.5} M_\odot$ at $0.2 \leq z < 0.4$ to construct galaxy model images. These model images are then used to simulate the images of high- z galaxies and test the recovery of A_O and D_O . Firstly, we apply median filtering to the *HST* images of the selected galaxies to suppress the noise in the images. A box of 6×6 pixels is adopted in the filtering, corresponding to 2 times FWHM of the *HST*/ACS *I*-band PSF ($\sim 0''.09$). A group of continuous adjacent pixels 0.8σ brighter than the background level in the original science image of a galaxy are taken as the galaxy's pixels. Here σ is the rms of the background noise. These pixels in the smoothed image are subtracted by 0.8σ to smooth the light profile at the edges and the rest pixels of the smoothed image are set to zero. Secondly, galaxy model images are scaled to simulate galaxies redshifted to $z \sim 0.3, 0.5$ and 0.9 , respectively.

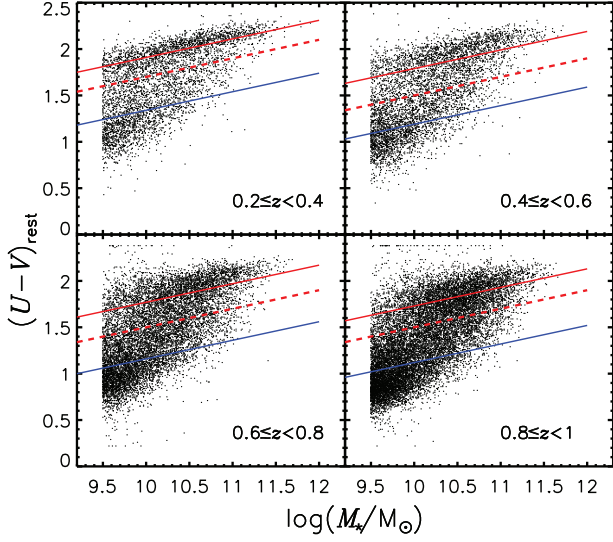


FIG. 2.— The rest-frame $U-V$ as a function of stellar mass for 35 076 galaxies with $M_* \geq 10^{9.5} M_\odot$ and $0.2 \leq z \leq 1$ in the COSMOS field. In each panel, the dashed line separates blue-cloud and red-sequence galaxies following Borch et al. (2006); and the red and blue solid lines are parallel to the dashed line and best fitting the two populations, respectively.

This is done by decreasing the size and surface brightness of the model galaxies and adding background noise into the images. Finally, A_0 and D_0 are derived from the images of the simulated high- z galaxies.

The software tool FERENGI (Full and Efficient Redshifting of Ensembles of Nearby Galaxy Images, Barden et al. 2008) is used to do simulations. To redshift a model galaxy to high z , one needs to correct for size downscaling, surface brightness dimming and band-shifting. The size degradation and brightness dimming can be directly calculated when the cosmology is given. Moreover, the intrinsic size evolution of galaxies since $z = 1$ (van der Wel et al. 2014) is considered in our simulation because galaxies are physically more compact in the past. Additionally, the evolution of stellar population in galaxies complicates the brightness estimate. Instead, we determine the brightness of a redshifted galaxy from real galaxies at the high z with the same stellar mass as the low- z galaxy. The counterparts at high z are identified to have the same location in the stellar mass versus rest-frame $U-V$ color diagram. Figure 2 shows the stellar mass versus rest-frame $U-V$ diagram of our sample of 35 076 galaxies from the UltraVISTA catalog. The blue-cloud and red-sequence galaxies are separated by the dashed line in each of four even redshift bins over $0.2 \leq z \leq 1$ following Borch et al. (2006). In each panel of Figure 2, the red and blue solid lines, parallel to the dashed line, describe the mass-color relations of two populations, respectively. At a fixed stellar mass, the offset from one mass-color relation normalized by the distance of the relation from the dashed line marks the location of a galaxy in the diagram. By doing so, we obtain locations of the selected 1178 galaxies used for simulations in the mass-color diagram of $0.2 \leq z < 0.4$. In each of the other three redshift bins ($z \sim 0.3, 0.5$ and 0.9), we select ten nearest real galaxies centered at each of the 1178 locations and take the median I -band magnitude of the ten galaxies as the brightness of the model galaxy to be simulated. In addition, photon noise is added into the model images of simulated high- z galaxies. The same sky background randomly selected from blank regions of the *HST/ACS I*-band images of COSMOS are also

combined with the model images. For each model galaxy, we create 16 background images and thus general 16 model images used for measuring A_0 and D_0 . Figure 3 presents the original science image of one example galaxy at low- z , in comparison with the smoothed profile and images of the same galaxy redshifted to $z \sim 0.5, 0.7$ and 0.9 .

The same configurations for *HST* images given in Section 2 are adopted to measure A_0 and D_0 from the images of simulated high- z galaxies with morphology known. Background noise of course affects the detection of signals from a simulated galaxy, in particular in the outskirts with low-surface brightness. Each simulated galaxy image is combined with 16 random background images to estimate errors in measured A_0 and D_0 caused by the background noise. We find marginal variations among measured A_0 and D_0 , suggesting that the measurements of the two structural parameters are reliable and show no dependence on the type of morphologies. The mean of 16 A_0 (D_0) measures is adopted for a simulated galaxy. Then we compare the measures of A_0 and D_0 at given redshifts with these derived from the (noise-free) model galaxy image. Figure 4 demonstrates the changes of measured A_0 and D_0 when model galaxies with different stellar masses are located at $z \sim 0.5$ (top), 0.7 (middle) and 0.9 (bottom). We can see that the changes of A_0 and D_0 are coupled with each other; and then changes become larger at increasing redshift and for lower mass galaxies. It is clear that the two parameters tend to be overestimated for galaxies with regular morphologies (intrinsically small in A_0 and D_0) and underestimated for those with disturbed morphologies (intrinsically large in A_0 and D_0). This is understandable because the relatively increasing contribution from noise easily increases A_0 (and D_0) for the regular galaxies when they become faint and less resolved at increasing redshift; however, the galaxies displaying irregular structures in their outskirts would appear more regular (measured A_0 and D_0 decreasing) as the faint asymmetric features become gradually undetectable at increasing redshift. And lower-mass galaxies are relatively more influenced by these effects. We conclude from Figure 4 that measures of A_0 and D_0 for high- z galaxies may be systematically biased in the sense that the spread of galaxies in both A_0 and D_0 would shrink to have more in the middle at increasing redshift. This suggests that part of high- z galaxies with disturbed morphologies would be missed in our A_0-D_0 selection and merging galaxies with faint tidal tails are barely detectable at high z . Bearing this in mind, we try to correct for the incompleteness to estimate the merger rate in Section 4.2.

4. MERGING GALAXIES WITH LONG TIDAL TAILS

4.1. Identification of Merging Galaxies with Tidal Tails

We measure A_0 and D_0 from *HST/ACS I*-band images for the complete sample of 35 076 galaxies with $\log(M_*/M_\odot) \geq 9.5$ and $0.2 \leq z \leq 1$ in the COSMOS field. The sample galaxies are divided into star-forming and quiescent galaxies using the *UVJ* method (Williams et al. 2009). Figure 5 presents the measurement results of A_0 and D_0 for the star-forming and quiescent galaxies split into 4 bins in stellar mass and 4 bins in redshift. The best-fit solid lines to subsamples of galaxies have similar slopes, indicating that the correlation between A_0 and D_0 is nearly uniform. As pointed out in Section 3.2, galaxies at $z > 0.4$ appear to be more concentrated in the A_0-D_0 space, especially for less massive galaxies. Still, we find that star forming galaxies have larger A_0 and D_0 than quiescent galaxies, which are usually smooth in morphology.

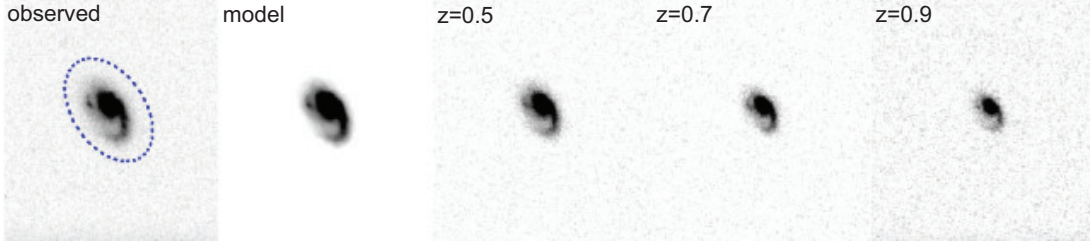


FIG. 3.— Image comparison of one example galaxy at $z = 0.37$ with the galaxy model (i.e. the smoothed profile), and the same galaxy redshifted to $z \sim 0.5, 0.7$ and 0.9 (from left to right). A tidal arm clearly seen in the original science image (left) gradually shrinks with increasing redshift, denoting that the low-surface-brightness features are hardly detectable for high- z galaxies. The blue dashed ellipse represents 1.5 times Petrosian radius of the target. The semi-major axis of such ellipse is 10.7 kpc and the semi-minor axis is 6.8 kpc.

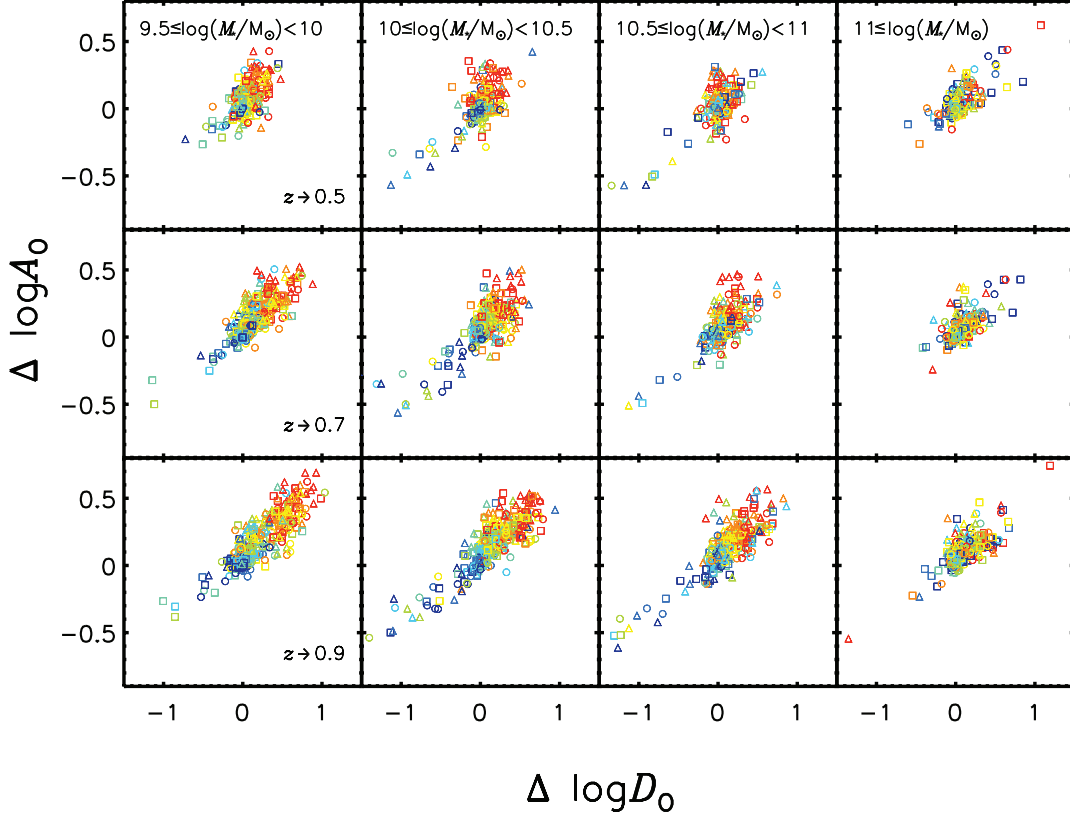


FIG. 4.— Deviations of measured A_O and D_O for same model galaxies at $z \sim 0.5$ (left), 0.7 (middle) and 0.9 (bottom). Mathematically, $\Delta \log A_O = \log A_O(z) - \log A_O(\text{model})$ and $\Delta \log D_O = \log D_O(z) - \log D_O(\text{model})$. Colors and symbols are same as in Figure 1.

Although some faint asymmetric features in galaxy outskirts are undetectable at high z , leading to the underestimate of A_O and D_O , these with measured A_O and D_O sufficiently high should have asymmetric structures detectable. We note that foreground or background sources may project next to target galaxies and result in false asymmetric structures. Such cases are removed in our visual examination.

We aim to estimate the rate of merging galaxies traced by tidal tails as a function of redshift. Wen et al. (2014) investigated the selection criterion for merging galaxies using the $A_O - D_O$ method, yielding that galaxies with long tidal tails satisfy $\log(A_O) = -2 \log(D_O) - 1.1$. We adopt the criterion in our analysis, shown as the dashed-dotted lines in Figure 5, and select 13 227 of 35 076 galaxies to be candidates for merging galaxies. The next step is to visually check morphologies of the 13 227 galaxies to identify merging galaxies with long tidal tails. We point out that the 13 227 galaxies must contain

mergers with other morphologies (e.g., Lackner et al. 2014) and a detailed analysis of these galaxies will be presented in a future work.

Due to the projection effect, a tidal tail may appear to be shorter. On the other hand, tidal tails rapidly grow during a merging process and the length of the tails is dependent on the stage of the merging process. In our examination, the length of a tail is measured from the edge of the host galaxy to the tip end of the tail. The edge is approximately determined by the isophotal ellipse of the host galaxy when the tails are masked. Because short tidal tails are often indistinguishable from spiral arms or tidal arms (tidally-disturbed spiral arms), we rather focus on long (or extended) tidal tails. Here the long tails refer to these with length equal to or longer than the diameter of their host galaxies. The visual identification of tidal tails is independently carried out by Z. Z. W and X. Z. Z. Totally 461 galaxies are confirmed by the two viewers with long tidal tails.

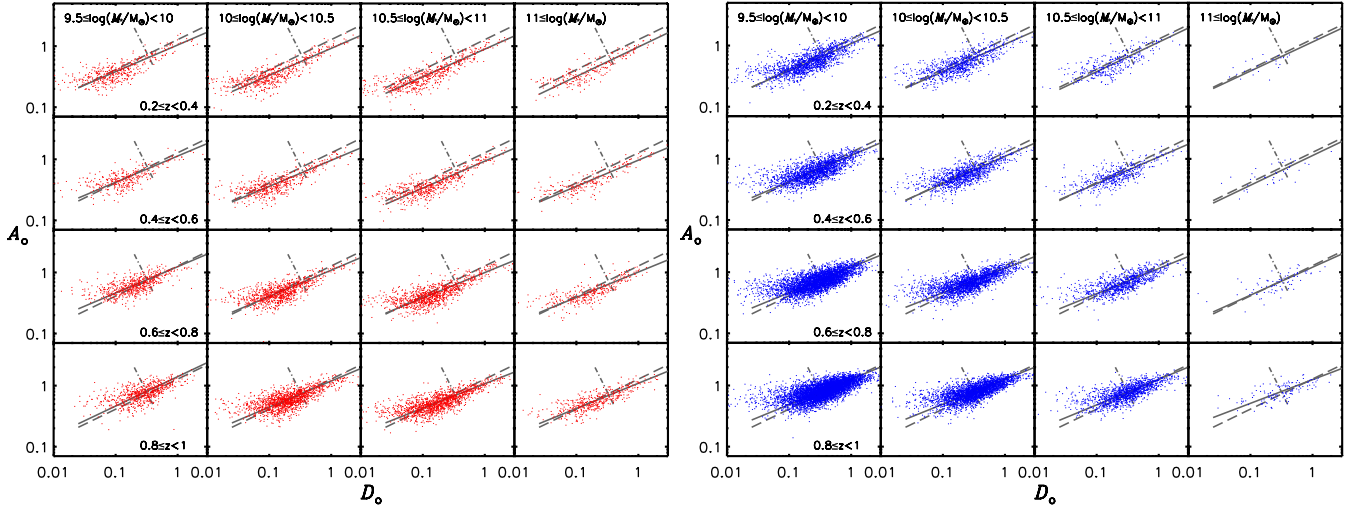


FIG. 5.— The $A_0 - D_0$ diagram of 35 076 galaxies from COSMOS split into 4 mass bins and 4 redshift bins. The left panels show quiescent galaxies (red) while the right panels show star-forming galaxies (blue). The solid line in each bin is the best fit to the data points. The dashed line represents the best fit of galaxies in the CDFS field from Wen et al. (2014). The dashed-dotted line gives the selection cut for galaxies with tidal tails (see the Appendix for more details).

Figure 6 illustrates 12 examples from the 461 galaxies. They are apparently merging systems with long tidal tails. We also show four examples of galaxies exhibiting tail-like structures in Figure 7. These structures are either spiral arms, accreting bridges from companions, or short tidal tails, and not included into our sample of long-tidal-tail systems.

In total 461 galaxies are identified to have long tidal tails from 13 227 merger candidates selected using the $A_0 - D_0$ technique from the parent sample of 35 076 galaxies with $\log(M_*/M_\odot) \geq 9.5$ and $0.2 \leq z \leq 1$ in the COSMOS field. The photometric catalogs of the 461 galaxies and their image stamps are electronically available online. We note that if two galaxies in a merging system are both resolved in the ground-based K_s -band catalog, they are counted as one merger event. The stellar mass of such a system is the sum of two components. We also find some of them to contain star clusters and tidal dwarf galaxy (TDG) candidates in their tidal tails. We refer massive compact clumps found in tidal tails to be TDG candidates. TDGs are self-gravitating, dark-matter-free systems formed by gravitational instability of pre-enriched gas clouds in tidal tails with size and mass comparable to classical dwarf galaxies (Braine et al. 2001; Weilbacher et al. 2003; Duc et al. 2004; Bournaud & Duc 2006; Wetzstein et al. 2007; Bournaud 2010; Wen et al. 2012). Due to the lack of multi-band high-resolution imaging data, we are unable to extract spectral energy distributions for the TDGs candidates and estimate stellar mass and properties of stellar population. Still, we provide a sample of 181 TDG candidates at intermediate redshifts, which can be used for further exploration.

The selected 461 merging galaxies with long tidal-tails are compared with the parent sample of galaxies in the $U - V$ versus $V - J$ color diagram, as shown in Figure 8. The grey data points represent quiescent and star-forming galaxies clearly separated into two regions in this plot. The 461 tidal-tailed galaxies with (without) TDG candidates are shown in black (green) solid circles. The adopted selection criteria for quiescent galaxies are derived from Williams et al. (2009). We can see that the solid circles widely spread in the region of star-forming galaxies, suggesting that the tidal-tail-selected merging galaxies originate from this population. Only twenty-four tidal-tailed systems fall into the region of quiescent galaxies, indicating that they are likely to be in the late stage of merging

with star formation quenched already. This result that tidal-tailed galaxies belonged to the star-forming galaxy population is consistent with our understanding of the tidal-tail creation in merger events involving disk galaxies that usually are forming stars. In contrast, mergers between two early-type galaxies often display diffuse tidal debris with no or only little star formation (e.g., Elmegreen et al. 2007a). The diffused structures are generally arc-like or plume-like, having similar colors as their host galaxies. Although such tidal structures may occasionally appear as tail-like in a special projection angle, mergers between early-type galaxies are still ignorable in a statistic sense (Duc & Renaud 2013).

Moreover, the I -band surface brightness distribution of identified tidal tails is given in Figure 9. The measurements are performed using the task *Polyphot* in IRAF. The surface brightness of tidal tails is within $22 - 24 \text{ mag arcsec}^{-2}$ at $z \sim 0.2$ down to $23 - 25 \text{ mag arcsec}^{-2}$ at $z \sim 1$ due to the surface brightness dimming effect. Only a few tidal tails are fainter than the 3σ surface brightness limit of $25.1 \text{ mag arcsec}^{-2}$. The surface brightness limit of the I -band imaging data is determined using aperture photometry in a blank sky area. The photometry is performed and repeated using an aperture of radius = 5 pixels ($\sim 1.5 \text{ PSF}$ size). As shown in Figure 9, nearly all the identified tidal tails have intrinsic surface brightness $< 23.1 \text{ mag arcsec}^{-2}$ in optical bands. Comparing with the detection limit of the I -band data, our selection of tidal tails becomes incomplete at high redshift. The incompleteness of tidal tail selection will be estimated through simulations (see Section 4.2) and corrected in merger rate calculation.

4.2. Estimate of Completeness

It is important to address the completeness of mergers with tidal tails selected by the $A_0 - D_0$ technique. Tidal tails of mergers at high z may be spatially resolved, but undetectable if they appear to be too fainter due to cosmological surface brightness dimming. From simulations presented in Section 3.2, we estimate the fractions of tailed galaxies that are not picked up by the $A_0 - D_0$ selection together with visual examination when the tailed galaxies at $0.2 < z < 0.4$ are redshifted to $z \sim 0.5, 0.7$ and 0.9 . Of 60 merging galaxies with long tidal tails, 47 (78%), 43 (72%) and 37 (62%)

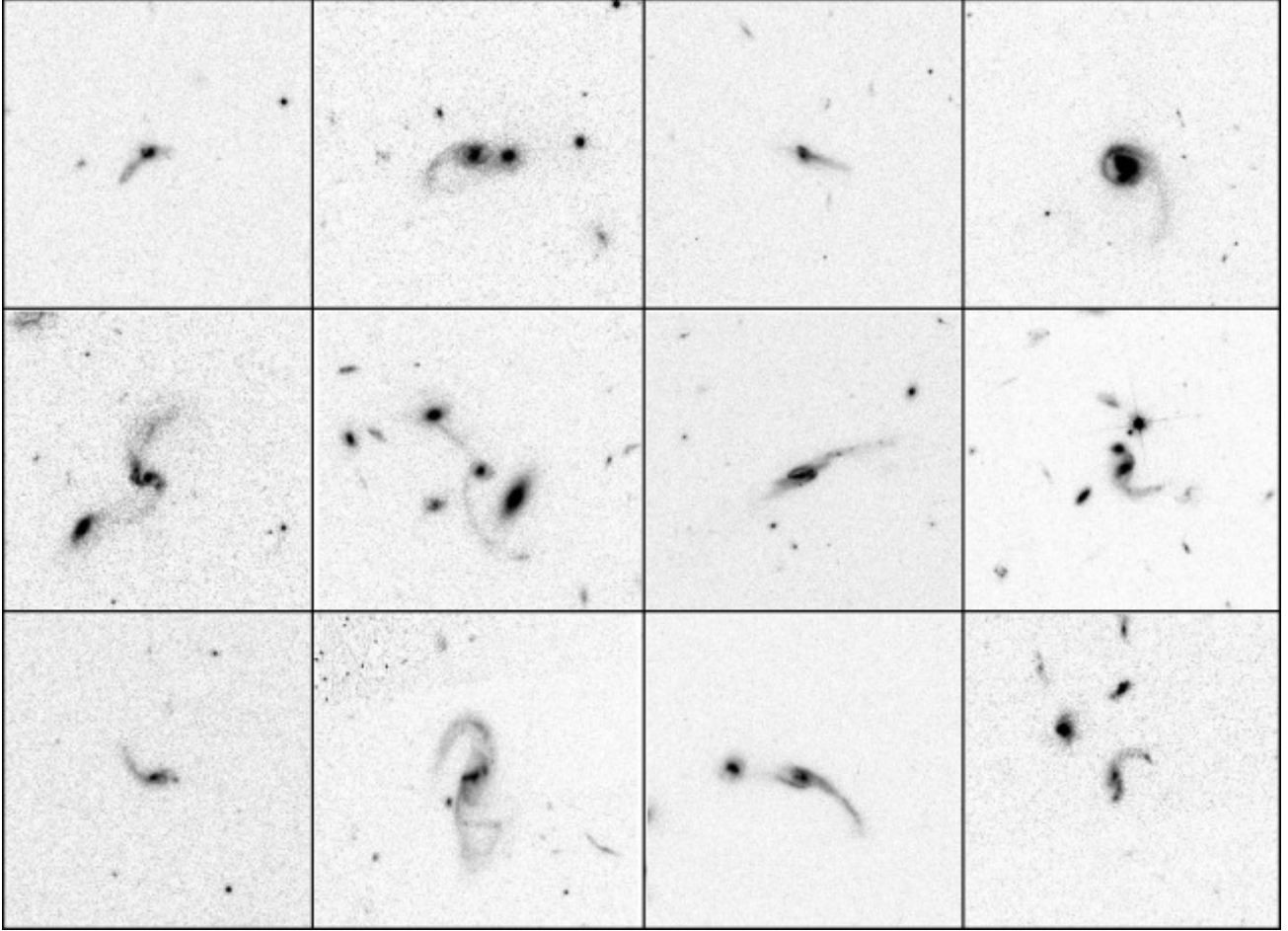


FIG. 6.— Examples of mergers with long tidal tails from COSMOS. These image stamps are given in a size of 120×120 kpc. All of the 461 stamps are available in the online material.

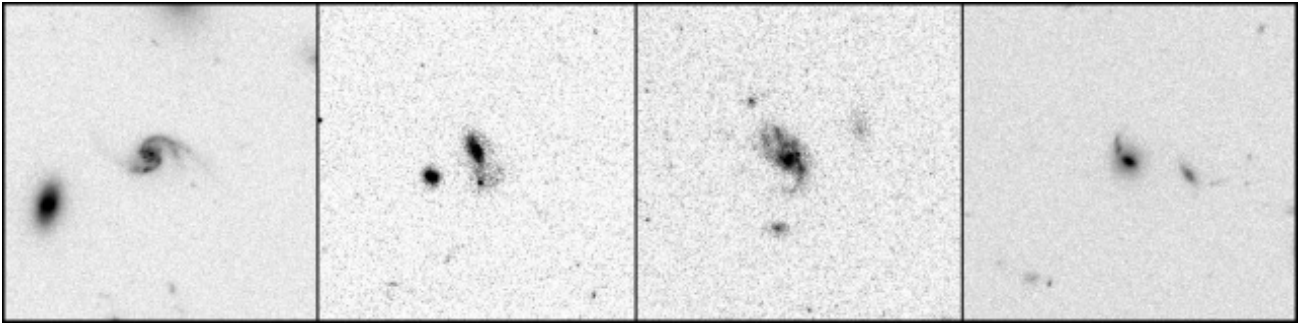


FIG. 7.— Examples of galaxies with tail-like structures (spiral arms, accreting bridges from companions, short tidal tails and debris related with early-type galaxies) but not long tidal tails. These image stamps are given in a size of 120×120 kpc.

TABLE 1
CATALOG OF MERGING GALAXIES WITH TIDAL TAILS

ID	RA (h m s)	Dec. (d m s)	z	$\log(M_*/M_\odot)$	M_I (mag)	M_{K_s} (mag)	$U-V$	$V-J$	D_O	A_O
218	10 01 38.323	01 38 27.50	0.94	10.2	23.0	21.1	1.52	1.05	1.27	1.20
708	10 01 34.615	01 39 57.87	0.60	9.66	20.5	19.8	0.40	0.51	1.40	1.31
737	10 02 32.352	01 39 59.63	0.85	10.1	21.6	20.5	0.97	0.81	0.57	1.04
939	10 02 21.446	01 40 21.89	1.00	10.4	21.6	20.1	0.97	0.79	0.39	0.86
...

NOTE. — This table is available in its entirety in the online material. A portion is shown here for guidance regarding its form and content.

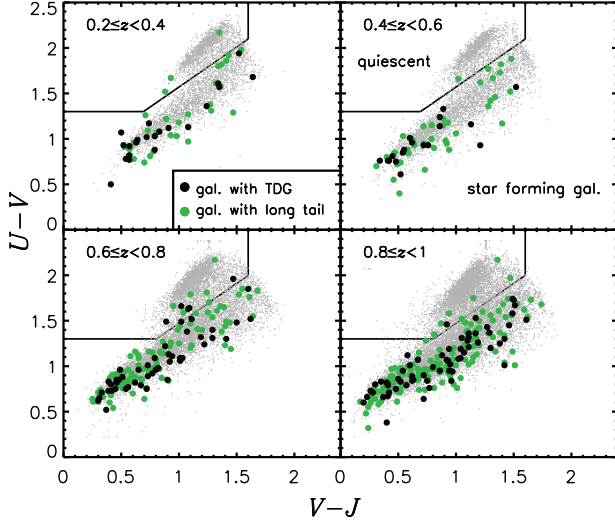


FIG. 8.— The $U-V$ Vs. $V-J$ diagram of 461 merging galaxies with long tidal tails (solid circles) in comparison with the parent sample of 35 076 galaxies (gray points). The black (green) circles represent mergers containing (or not) tidal dwarf galaxy candidates. The solid lines show the adopted division between the star-forming and quiescent galaxies in each redshift bin.

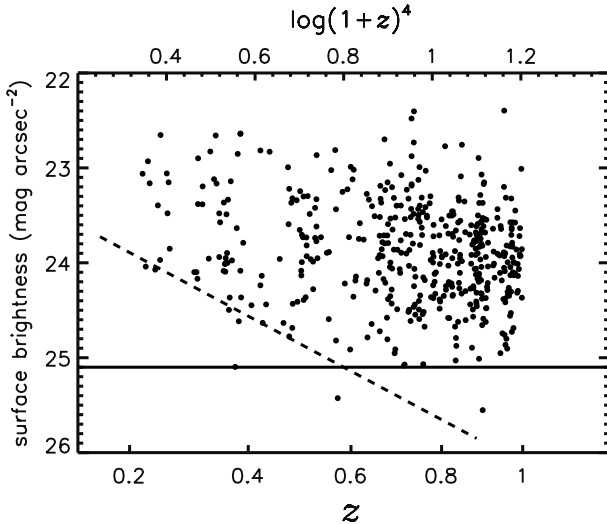


FIG. 9.— The I -band surface brightness of 461 tidal tails. The solid line gives the 3σ surface brightness limit. The dashed line shows the cosmic dimming as $\sim(1+z)^4$ for a tidal tail with intrinsic surface brightness of $23.1 \text{ mag arcsec}^{-2}$ in optical bands.

are recovered as the tailed ones at $z \sim 0.5, 0.7$ and 0.9 , respectively. We use these fractions to correct for the incompleteness in estimating occurrence rate of mergers with long tidal tails. It is worth noting that the estimation of completeness is based on two assumptions: (1) The intrinsic surface brightness distribution of tidal tails is not changed significantly across $0.2 < z < 1$ (see Section 4.1); (2) The completeness of tidal tails at the lowest redshift bin $z \sim 0.3$ is 100% and the fractions estimated at higher redshift are relative to the completeness at $z \sim 0.3$.

5. GALAXY MERGER RATE

Long tidal tails are most likely produced in major mergers of two parent galaxies and at least one disk galaxy is involved (Duc & Renaud 2013). Stars in the parent disk galaxy had ordered motions (i.e., following a common rotational veloc-

ity pattern) around the spin axis. Tidal force from companion may change the dynamics of the stars in the same way and thus form prominent tidal features like tails after the first pericenter passage of galaxy encounter. However, stars in pressure supported galaxies (e.g., ellipticals) fail to follow a uniform motion when external tidal force is applied. Therefore, only diffused tidal debris formed in the merger between two early-type galaxies.

As explored by numerical simulations (Barnes 1992; Howard et al. 1993; Mihos & Hernquist 1996; Duc & Renaud 2013; Barnes 2016), characterization of the tidal tails is strongly correlated with the orbital parameters (e.g. spin and orbital angular momentum) of the mergers. In the case of a planar prograde encounter, the spin and the orbital motion are coupled (zero-inclination) and the strongest tidal tail can be created. As the disk inclination angle increases, the tails tend to be more warped. In the case of planar retrograde encounter, only weak tidal features can be formed. The galactic disks often exhibit short-lived ripple-like features instead of a tidal bridge or tail. Meanwhile, highly-warped and diffused structures can be formed in highly-inclined retrograde encounter. Only at extreme conditions, the polar encounter could create a tail-like broad and straight tidal feature. In this work, mergers are identified based on their long tidal tails, indicating that the mergers selected are most likely undergoing prograde encounters and bias against retrograde encounters.

5.1. Galaxy Merger Fraction

Using the sample of 461 merging galaxies with long tidal tails, we estimate the fraction of such galaxies among the galaxies of similar stellar mass and redshift. Using the completeness corrections presented in Section 4.2, we estimate the merger fraction of galaxies with stellar mass $\geq 10^{9.5} M_\odot$. The numbers of tailed galaxies in different stellar mass and redshift bins are listed in Table 2. The merger fractions that are corrected for surface brightness incompleteness are also shown in Figure 10. We find that merger fraction appears to be higher at higher redshifts, consistent with the theoretical predictions from the hierarchical cosmology (Hopkins et al. 2010). The evolution of merger fraction with redshift can be fitted by a power-law function in the form of $f = f_0(1+z)^m$. We adopt the Monte Carlo method to take the uncertainties of data points into account and derive the best-fit parameters of the function from 3 000 fits using the least squares method, yielding $m = 2.0 \pm 0.4$ and $f_0 = 0.64 \pm 0.13$ percent. Moreover, our results reveal that merger fraction is dependent on galaxy stellar mass, as shown in Figure 10, in the sense that less massive galaxies exhibit a higher fraction of mergers than massive galaxies out to $z = 1$, although uncertainties are relatively large.

5.2. Galaxy Merger Rate

Galaxy merger rate is usually described in two ways. One is the fractional merger rate \mathcal{R} that traces the number of mergers that one galaxy would undergo in unit time, given by

$$\mathcal{R} = f_m / T_m. \quad (3)$$

The other is the merger rate Γ in units of number of mergers per unit time per unit co-moving volume:

$$\Gamma = n_{\text{gal}} * f_m / T_m. \quad (4)$$

Here f_m is galaxy merger fraction, T_m is the average detection timescale during which the merger is selected by a specific

TABLE 2
NUMBERS OF MERGERS AND GALAXIES

z	$\log(M_*/M_\odot)$				N_{tot}	Completeness	Corrected Merger Fraction [%]
	9.5–10	10–10.5	10.5–11	> 11			
0.2–0.4	27/1951	14/1387	9/881	1/270	51/4489	1	1.1 ± 0.16
0.4–0.6	30/2353	19/1662	5/1019	2/257	56/5291	0.78	1.4 ± 0.18
0.6–0.8	69/4606	47/3328	19/1972	6/403	141/10309	0.72	1.9 ± 0.16
0.8–1.0	101/6618	63/4815	42/2923	7/631	213/14987	0.62	2.4 ± 0.17

NOTE. — Numbers of merging galaxies with long tidal tails and parent galaxies in stellar mass and redshift bins. The errors are inferred from poisson uncertainties of the numbers of tailed galaxies and parent galaxies through error propagation. Noting that the sample completeness is 95% for galaxies in the lowest mass bin at $z \sim 0.9$. Such uncertainty is also considered in error estimation.

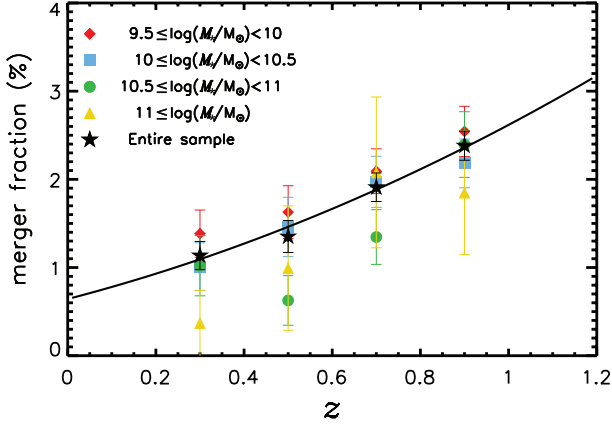


FIG. 10.— Fraction of merging galaxies with tidal tails as a function of redshift. The colored points represent the galaxies with different stellar mass while the black points give the fraction of the tailed mergers over entire mass range. The best-fit power-law function to the black data points are given as $(1+z)^m$ where $m = 2.0 \pm 0.4$.

technique, and n_{gal} is the number density of galaxies in the co-moving volume at a given redshift. Although the merger rate Γ provides a direct measure of merging events in the framework of galaxy formation and evolution, it suffers from large uncertainties as n_{gal} varies from field to field due to the cosmic variance. The fractional merger rate \mathcal{R} was often presented in the literature. We also estimate the fractional merger rate using our sample of tailed galaxies.

The detection timescale T_m is a key parameter for determining merger rate of galaxies. In this work, major mergers are traced by long tidal tails and the duration for displaying long tidal tails in merger processes is thus used as T_m . The duration can be determined from merger simulations. From the simulations by Conselice (2006), we carefully investigate the snapshots of mergers between equal-mass disk galaxies. Long tidal tails are visible when the host galaxies reach their maximal separation (0.68 Gyr) and can be still seen at 1.2 Gyr when disk progenitors have merged as a single system. However, they become invisible at 1.33 Gyr, suggesting that duration for displaying long tidal tails is around 0.5 Gyr or longer. Meanwhile, some simulations gave durations for long tidal tails, ranging from about 0.25 Gyr (Bournaud & Duc 2006; Bournaud et al. 2011) to 0.77 Gyr (Ji et al. 2014). Finally, we adopt 0.5 ± 0.25 Gyr to be the duration for displaying long tidal tails in major mergers. It is worth noting that identifying long tidal tails in snapshots is dependent on the viewing angle. An averaged duration for long tidal tail appearance over viewing angles would improve the estimate of duration.

Jogee et al. (2009) adopted $T_m \sim 0.5 - 0.8$ Gyr for visually selected gas-rich mergers. The adopted timescale of tailed mergers in this work is the lower limit of that in Jogee et

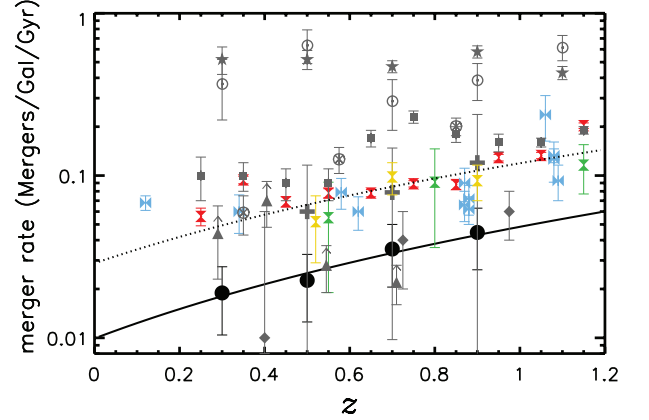


FIG. 11.— The major merger rate of galaxies with $\log(M_*/M_\odot) \geq 10$ as a function of redshift in comparison with representative results from the literature. All the grey symbols refer to merger rates based on disturbed morphologies while the colored symbols represent merger rates based on close pairs. Our results are given in black solid circles best-fitted by $\propto (1+z)^{2.3 \pm 1.4}$. Red hourglass: Kartaltepe et al. (2007); Blue hourglass: Lin et al. (2008); Yellow hourglass: de Ravel et al. (2009); Green hourglass: Bundy et al. (2009); Grey solar: Lotz et al. (2008b); Grey triangle: Jogee et al. (2009); Grey star: Shi et al. (2009); Grey diamond: López-Sanjuan et al. (2009); Grey square: Conselice et al. (2009); Grey plus: B10. Grey circle with cross: Lackner et al. (2014). Merger rates in the literature are derived from Lotz et al. (2011) if available. The dotted line represents the best fitting line to all the measurements on close galaxy pairs.

al. (2009) for that tidal tails only account for a certain merging stage. In addition, a longer timescale (0.8 Gyr) is used in B10, aimed at accounting for longer merger stage from close-pair with tidal bridges to the later coalescence stage exhibiting long tidal tails.

Merger rate is dependent on galaxy stellar mass (Lotz et al. 2011). We further focus on merger rate among galaxies with $\log(M_*/M_\odot) \geq 10$ and compare our results with those based on the samples selected by the same mass cut. Figure 11 shows our results of fractional merger rate as a function of redshift, in comparison with representative results from previous works described in Section 6. The major merger rate we derived evolves mildly with redshift, and is best described by $R_0(1+z)^{2.3 \pm 1.4} \text{ Gyr}^{-1}$ where $R_0 = 0.01 \pm 0.007$. We notice that our data points are generally lower than the merger rates derived from galaxy pairs or disturbed morphologies. This systematic offset can be explained by the merger identification bias. Our sample of major mergers traced by long tidal tails is biased against mergers without tidal tails such as mergers between two early-type galaxies. Therefore our major merger rate accounts for only a fraction of merger rate in each redshift bin. The discrepancy of our measurements from the others are partly due to the sample selection and cosmic variance. We come back to discuss this issue in next section.

We compute the number of expected mergers for a local galaxy undergoing over a given cosmic period using

$$N = \int_{t_1}^{t_2} \frac{1}{\Gamma(z)} dt = \int_{z_1}^{z_2} \frac{1}{\Gamma(z)} \frac{t_H}{(1+z)} \frac{dz}{E(z)}, \quad (5)$$

where $\Gamma(z)$ is the duration that a galaxy exists before undergoing a merger as a function of redshift, t_H is the Hubble time, and $E(z) = [\Omega_M(1+z)^3 + \Omega_k(1+z)^2 + \Omega_\Lambda]^{-1/2} = H^{-1}(z)$ (Hogg 1999; Conselice et al. 2009). We derive that a galaxy would undergo about 0.3 wet major mergers since $z = 1$ to the present day from our measurements or 2.9 wet mergers when the merger rate is extrapolated to $z = 2$.

6. DISCUSSION

Tidal tails are solid indicator for major merger systems in which at least one disk galaxy is involved. The mergers of two early-type galaxies hardly generate such features (Duc & Renaud 2013). The merger rate from this work accounts only for merging galaxies with long tidal tails, corresponding to a special type among a variety of mergers classified by morphology (and merging stage). Then the question is what fraction of overall galaxy major mergers display long tidal tails? We discuss the representative measurements of galaxy merger rate from the literature and our measurement respectively, and try to draw an answer to this question.

6.1. Measurements of Merger Rate from Previous Works

Many studies have been contributed to the measurement of merger fraction of galaxies using a variety of selection techniques, incompleteness corrections and parent galaxy samples. An agreement has been reached between these studies, giving that galaxy merger fraction globally increases with redshift. Still, significant discrepancy can be seen between different measurements.

In Figure 11 we collect representative measurements of merger rate corrected to roughly the same mass selection $\log(M_*/M_\odot) \geq 10$ and ensure the merger rates are measured approximately from the same galaxy population. It is worth noting that evolving luminosity cuts are performed for sample selection in the literature (e.g., $M_V < -19.8 - 1.0z$ Kartaltepe et al. 2007; Lin et al. 2008; Shi et al. 2009). The luminosity cuts are based on a model of passive luminosity evolution (PLE) of galaxies. Lotz et al. (2011) argued that such cuts may select similar galaxy population as those derived through a fixed stellar-mass cut $M_* \geq 10^{10} M_\odot$. We thus include their results in Figure 11 for comparison. We caution that major merger rates from Jogee et al. (2009) and Lackner et al. (2014) in the Figure 11 are based on a sample of galaxy with $M_* \geq 2.5 \times 10^{10} M_\odot$ and $M_* \geq 10^{10.6} M_\odot$. We caution that their selection cuts are higher than ours, although we include these results for comparison.

We can see that merger rates of close pairs are consistent with each other within the uncertainties, and the global merger rate can be best fitted by $0.03 \pm 0.002(1+z)^{2.0 \pm 0.1}$. This indicates that a galaxy would undergo 0.8 major (wet+dry) mergers since $z = 1$, about 2.5 times higher than our measurement on mergers with tidal tails. Note that the merger rates of close pairs are converted from pair fractions (f_{pair}) instead of fractions of galaxies in pairs (N_c) (Lotz et al. 2011), allowing comparison with merger rates from morphology studies. For this reason, two galaxies linked by a tidal bridge are counted as one merger event in this work. On the other hand,

merger rate derived using morphological techniques are usually higher than those derived from close pairs. This is because the morphological selection for major mergers may be contaminated by minor mergers. Furthermore, galaxy pairs are early-stage mergers and thus correspond to progenitors of disturbed merging galaxies. Galaxies in morphological studies will be less massive or fainter than galaxies in pair studies if a uniform stellar-mass or brightness limit is adopted for sample selection. We should keep this in mind when merger rates of galaxies with disturbed morphology are directly compared with merger rates of pairs.

6.2. Merger Rate of Tidal-Tailed Galaxies

Using the $A_0 - D_0$ technique together with visual examination, we identify 461 galaxies having long tidal tails among 35 076 galaxies with $\log(M_*/M_\odot) \geq 9.5$ and $0.2 \leq z \leq 1$ in the COSMOS field. The tidal tails are known as low-surface-brightness features and hardly detectable at high z due to the cosmic dimming effect. By redshifting a sample of model galaxies constructed from low- z ones with a diversity of morphologies, we quantify the systematic biases in the measurements of the morphological parameters A_0 and D_0 at three redshifts $z \sim 0.3, 0.5$ and 0.9 . The corrections for the incompleteness in detection of tidal tails are derived through simulations and applied to the measured numbers of mergers listed in Table 2 to obtain the merger fractions in different stellar mass and redshift bins. Adopting an average detection timescale of 0.5 Gyr, the merger fractions can be converted into merger rates. As shown in Figure 10, our results reveal that the merger fraction of tidal-tailed galaxies mildly increases with redshift following $\propto (1+z)^{2.0 \pm 0.4}$, and less massive galaxies contain a higher fraction of tailed mergers than massive ones at all cosmic epochs examined.

The increase of galaxy fraction with redshift is generally consistent with the most measurements listed in Section 6.1. Moreover, the dependence of merger fraction on stellar mass (or luminosity) are also reported in previous works (e.g., Lin et al. 2004; Bundy et al. 2005, 2009; de Ravel et al. 2009; B10). However, the measurements based on close pairs (e.g., Bundy et al. 2009) favor the opposite that massive galaxies are more likely to host companions than less massive galaxies. A possible reason for this discrepancy is the bias in pair identification due to the strong clustering effect (i.e., galaxies reside in groups or clusters but are assumed to merge, Kitzbichler & White 2008). Another reason could be due to the cosmic variance as the sample used in Bundy et al. (2009) is rather small and probably leave large uncertainties in their results.

The results shown in Figure 10 implies the merger fraction of massive galaxies increases more rapidly with redshift than less massive galaxies. The best-fit power index m is 1.6, 2.1, 3.5 and 5.0 for galaxy mass bins from the low- to high-mass end, respectively. This predicts that merger fraction of massive galaxies would become higher than that of less massive galaxies at $z > 1$, consistent with the findings from previous studies (e.g., Conselice et al. 2008; B10). Moreover, we stress that merger fraction of galaxies with $10^{9.5} M_\odot \leq M_* < 10^{10} M_\odot$ at $0.8 \leq z \leq 1$ may probably be underestimated due to the difficulties in finding faint tidal tails in visual examination of low-mass galaxies at $z \sim 0.9$. The underestimation of merger fraction may result in a lower m for the lowest-mass bin. The sample completeness of the lowest-mass bin is relatively larger although the global completeness galaxies at $M_* \geq 10^{9.5} M_\odot$ and $z = 1$ is estimated to be about

95%. This also increases the uncertainties of merger fraction for low-mass galaxies.

B10 used similar probes (tidal tails and bridges) to identify galaxy mergers. We notice that their merger fraction is substantially higher and evolve more rapidly with redshift than our results. The discrepancy may be attributed to several reasons. First, more than one third of the mergers identified in B10 are not included in our statistics. These mergers either display a tidal bridge linking one galaxy to the other or double cores but no tail is presented. Second, a close pair of galaxies with tidal tails is counted as one merging event in our analysis. Such system is seen as two mergers in B10 if a bridge is shown, leading to roughly another 3% enhancement of their merger rate. Moreover, the parent sample in B10 is selected using both stellar mass and brightness cuts. We argue that the brightness cut may lead to strong bias in particularly at high z . Star formation triggered by wet mergers can enhance the brightness of the host galaxies. A brightness selection would favor the detection of star-forming galaxies and possibly more mergers.

Galaxy pairs can be divided into early-type galaxy pairs, late-type galaxy pairs and mixed pairs. Mergers between two gas-poor early-type galaxies (dry mergers) are thought to be a major channel for the assembly of massive ($M_* \geq 10^{11} M_\odot$) galaxies at $z < 1$ (Bell et al. 2006; van Dokkum 2005; Buitrago et al. 2013; Conselice 2014). But early-type galaxy pairs contribute little to the total number of galaxy pairs, from $\sim 25\%$ in the present day to $\sim 10\%$ at $z \sim 1$ (e.g., de Ravel et al. 2009). Figure 11 presents the comparison of the merger rate of tidal-tailed galaxies with the global merger rate derived from close galaxy pairs in the literature (see Section 6.1). We find that the merger rate of tailed galaxies roughly accounts for a half of the global merger rate when the contribution of early-type galaxy pairs are removed. We conclude from Figure 11 that roughly half of disk-involved major mergers have undergone a phase exhibiting long tidal tails at $z < 1$.

The absence of tidal tail in disk-involved mergers may be attributed to special orbital parameters. For instance, long tidal tails are preferentially formed in prograde encounters where the spin of a disk aligns with the orbital spin. However, only weak, warped tails can be generated in retrograde encounters. Therefore, our merger sample is biased against retrograde mergers. In the case of head-on collision (with impact parameter of zero) between a disk and a compact spheroid galaxy, ring-like debris instead of tidal tail forms and radially expands due to the density wave created by the interaction (Mapelli & Mayer 2012; Fiacconi et al. 2012). The head-on collisions are not commonly seen and Arp 147 (Fogarty et al. 2011) and 2MASX J06470249+4554022, dubbed as “Auriga’s Wheel” (Conn et al. 2011) are two of this kind. On the other hand, in our work tidal tails are identified if they are longer than the diameters of their hosts. This implies that tidal tails with fixed lengths are easily selected in small galaxies and thus our selection probably misses some tidal tails in larger galaxies. In addition, a tidal tail could not be identified if its orientation is nearly coincident with the line of sight and appears to be much shortened due to the projection effect.

Tidal tails of mergers at $z > 2$ might be quite different from their local counterparts. Representative disk galaxies at $z > 2$ contain a few kpc-scaled blue spheroids on their disks and have clumpy morphology (Elmegreen et al. 2004, 2007b, 2009). The formation of the clumpy disks might re-

sult from the gravitational instability and fragmentation in gas-rich disks which are continuously fed by cosmological streams (e.g., Immeli et al. 2004a,b; Dekel et al. 2009). Simulations predicted that ongoing mergers of these galaxies will form clumps and filaments in the intergalactic space instead of long tidal tails as what observed in lower redshifts (Bournaud et al. 2011). It is worth noting that the formation of tidal tails might not be common during the disk-disk mergers at $z > 2$ and care should be taken when counting mergers with tidal tails in those cosmic epochs.

7. CONCLUSION

We carry out a careful morphological analysis using deep *HST*/ACS F814W imaging data for a complete sample of 35 076 galaxies with $M_* \geq 10^{9.5} M_\odot$ at $0.2 \leq z \leq 1$ selected from the UltraVISTA catalog of the COSMOS field. Two newly developed morphological parameters, the outer asymmetry A_0 and the outer centroid deviation D_0 are measured from galaxy images to probe asymmetric features in the outskirts of galaxies. The sample galaxies of different morphological types form a tight sequence in the $A_0 - D_0$ diagram, showing that the degree of morphological disturbance globally increases with A_0 and D_0 and these with highly-irregular structures occupy the high-value end. Merging galaxies with long tidal tails are pre-selected using the $A_0 - D_0$ selection technique, and further identified through visual examination. This type of galaxies are believed to be major mergers involving at least one disk galaxy. How the cosmic surface brightness dimming effects on the measurements of the two parameters are quantitatively estimated through simulations and the detection completeness for tidal-tailed galaxies are derived accordingly. We summarize our results as follows:

1. We find that the widely-used morphological parameter, asymmetry A , is significantly biased by the noise in the outskirts of a galaxy due to an incorrect treatment of the background subtraction. We provide a revised definition of A by including corrections for noise contamination. We also update the equation for computing the outer asymmetry A_0 and correct for the noise term. Details are given in the Appendix A.
2. Simulations are performed to quantify the effects of the cosmic surface brightness dimming on the measurements of A_0 and D_0 as a function of redshift, giving that the two parameters would be overestimated for galaxies with regular morphologies (intrinsically small in A_0 and D_0) and be underestimated for those with disturbed morphologies (intrinsically large in A_0 and D_0). The degree of the estimate bias is inversely correlated with galaxy stellar mass (and luminosity). The simulations suggest that 78, 72 and 62 percents of long tidal tails are detectable with the COSMOS *HST*/ACS images at $z \sim 0.5, 0.7$ and 0.9 , respectively.
3. In total 461 galaxies are identified to have long tidal tails from 13 227 merger candidates selected using the $A_0 - D_0$ technique from the parent sample of 35 076 galaxies over $0.2 \leq z \leq 1$. These galaxies spread in the same region as star-forming galaxies in the $U - V$ and $V - J$ diagram, confirming that tidal-tailed galaxies originate from the population of star-forming galaxies with morphologies dominated by disks.

4. We show that the fraction of mergers with long tidal tails evolves mildly with redshift following a power-law function $f = 0.64 \pm 0.13\% (1+z)^{2.0 \pm 0.4}$ out to $z = 1$. We also find that the tidal-tailed merger fraction is higher for less massive galaxies. However, merger fraction of massive sample evolves more strongly with redshift, indicating higher merger fraction of massive sample at $z \geq 1$. These are consistent with the results from previous studies.
5. Adopting an average detection timescale of 0.5 Gyr for tidal-tail-traced mergers, we obtain the evolution of the merger rate of such type of merging galaxies as $0.01 \pm 0.007(1+z)^{2.3 \pm 1.4} \text{ Gyr}^{-1}$. Combined with the global merger rate derived from close pairs, we find that nearly half of disk-involved major mergers at $z < 1$ have undergone a phase with long tidal tails. We infer

that a present-day galaxy would undergo about 0.3 major mergers creating long tidal tails since $z = 1$, roughly one-third of the total budget of major mergers.

We thank the referee for his/her constructive suggestions and comments, which greatly improve our manuscript. We thank Jeniefer Lotz for helpful suggestions during the conference *The Many Pathways to Galaxy Growth* in 2015. We also thank Cong Ma for the meaningful discussion on improving the non-parametric method. This work is supported by National Basic Research Program of China (973 Program 2013CB834900), the Strategic Priority Research Program “The Emergence of Cosmological Structures” of the Chinese Academy of Sciences (grant No. XDB09000000) and NSFC grant (U1331110).

APPENDIX

One challenge for the non-parametric methods is how to get rid of noise contamination. The Gini coefficient is strongly dependent on the noise level of imaging data and suffers from large uncertainties when signal-to-noise ratio is not sufficiently high (Lisker 2008). For asymmetry A , noise contribution is estimated by measuring A on a nearby blank sky region with the same aperture. However, the noise correction for A overestimates the real noise contribution (see Figure 1 in Shi et al. 2009). Here we present a detailed analysis on the noise effects in quantifying A and introduce a revised correction for noise contamination.

We construct a sample of model galaxies for testing the morphological parameter A . The sample consists of 569 isolated galaxies from Wen et al. (2014) (see Section 3.2 for more details about model generation). An artificial image is obtained through combining a model galaxy image with a background noise image. The parameter A is measured from both the artificial image and the noise-free model image following the definition given in Conselice (2003) as

$$A = \frac{\min(\sum |I_0 - I_{180}|)}{\sum |I_0|} - \frac{\min(\sum |B_0 - B_{180}|)}{\sum |I_0|}, \quad (1)$$

where I_0 is the intensity of the galaxy and I_{180} is the 180°-rotated intensity. The second term refers to the correction for noise contamination. A group of pixels are randomly selected from the background regions to form the background noise image. In the measurement, an aperture of 1.5 times the circular Petrosian aperture is adopted to estimate the noise contamination. Figure 12 presents comparison of the measure of A from noise-added and noise-free images for the 569 model galaxies. We find that noise contamination leads A to be systematically overestimated and the significant scatter indicates the uncertainties of noise contribution which is about 20% for a high-S/N galaxy and reaches 50% for a low-S/N galaxy (Shi et al. 2009). The noise correction introduced in Conselice (2003) overestimates the noise contamination and biases A to be smaller. This is because that all background pixels within the Petrosian aperture are used to calculate the noise contamination. As discussed in next section, however, we argue that noise contamination is correlated with the number fraction of noise dominated pixels of a galaxy indicating that only a part of the noise contribution estimated by Equation 1 is real. Furthermore, the measured A from noise-added images is found to be lower than that from noise-free model images in a few cases even if no noise correction is adopted. This is because that noise dramatically changes the segmentation maps of the model galaxies. In our measurements, only pixels within 1.5 times the circular Petrosian aperture are counted to calculate A and the extended structures of the model galaxies out of the aperture are ignored, leading to an underestimation in A . For a noise-free model galaxy image, all pixels associated with the galaxy are used to compute A .

A Revised Noise Correction for Rotational Asymmetry

To calculate A of a galaxy, one needs to measure the signal remained in the residual image relative to that in the scientific image. Mathematically, the modules of pixels in each image are derived and then the summation is performed. Pixels dominated by random noise likely significantly contribute to the summation even if little signal is included. As a consequence, different outputs are generated from noise-added image of a galaxy and the noise-free model. For a luminous galaxy that all pixels are brighter than 3σ of the noise, equivalent outputs are generated from the noise-added image and the model galaxy. It is thus important to quantify the number fraction of noise dominated pixels in the image of a galaxy against those signal dominated. In practice, 1σ of noise level is adopted as the criterion for the classification. The noise level is measured independently from the background.

The updated equation of A is given by

$$A = \frac{\min(\sum |I_0 - I_{180}|) - \delta_2}{\sum |I_0| - \delta_1}, \quad (2)$$

where $\delta_1 = f_1 * \sum |B_0|$, $f_1 = N_{flux < 1\sigma} / N_{\text{all}}$, $\delta_2 = f_2 * \min(\sum |B_0 - B_{180}|)$ and $f_2 = N_{|flux| < \sqrt{2}\sigma} / N'_{\text{all}}$. Parameters δ_1 and δ_2 measure the noise contributions within the I_0 and the residual image $I_0 - I_{180}$ respectively. Parameters f_1 and f_2 give the number fractions of noise dominated pixels relative to the total while N_{all} and N'_{all} mark the total number of pixels assigned to the galaxy in I_0 and

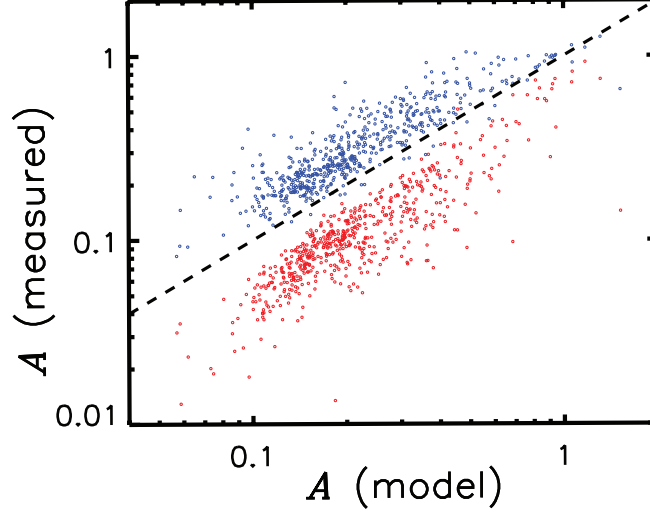


FIG. 12.— Comparison of asymmetry measurements from galaxy images with and without noise. Asymmetry of the noise-free model image is marked as $A(\text{model})$. For galaxy image with noise, the measurement of A is biased, as denoted by the blue data points (no correction for noise contamination). Red data points show the measurements of A after including correction for the noise contamination introduced by Conselice (2003). It is clearly that the noise correction leaves A underestimated. The dashed line indicates the 1:1 relation between $A(\text{measured})$ and $A(\text{model})$.

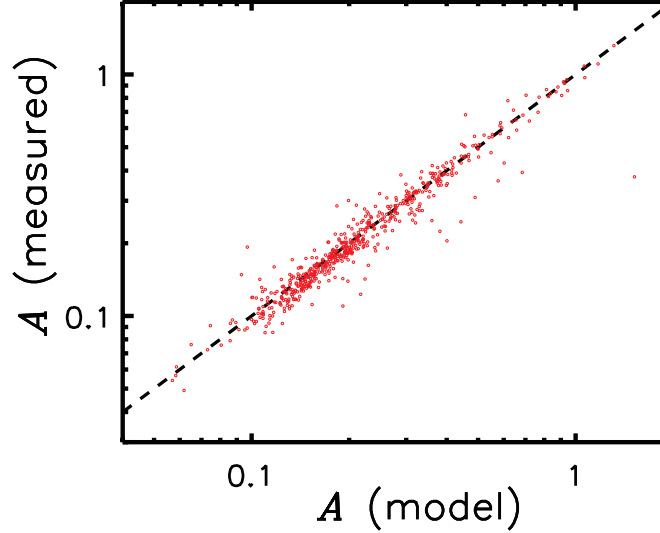


FIG. 13.— This figure compares the new measurements of A from noise-added images with the measurements from the models. The dashed line indicates the 1:1 relation between $A(\text{measured})$ and $A(\text{model})$.

the residual image. Parameter σ is the standard deviation of noise in I_0 . Moreover, the residual image is derived by combining I_0 with $-I_{180}$ where image of gaussian distributed noise as well as its 180° -rotated version are overlapped on. The standard deviation of the noise in the residual image increases by a factor of $\sqrt{2}$ relative to that in the I_0 . For this reason, pixels within $\pm\sqrt{2}\sigma$ are defined as noise dominated pixels in the residual image.

The size of a galaxy is determined by the Petrosian aperture and the pixels within 1.5 times the elliptical Petrosian aperture of the galaxy are used to compute A . Elliptical apertures more closely follow the light profile of galaxies than circular apertures, especially for edge-on disks. The rotational centers of either model galaxies, background images or artificial galaxies are determined by an iterative process respectively. The initial center (usually the flux-weighted centroid of a galaxy) together with the eight pixels surrounded will be tested in turn until the minimum value of asymmetry is found.

Figure 13 compares the new measurements of A from noise-added images with the measurements from the models. The new measurements of A are in line with the initial values of the models. Only $< 5\%$ cases show large offsets from the initial A . In these cases, extended structures out of the 1.5 times elliptical Petrosian radius of an artificial galaxy are not included in the measurements but they are included when the initial A of the model is measured. The determination of rotational center of the artificial galaxy thus deviates from that of the model galaxy. We also notice that the slope of the data-points in Figure 13 will change if the criterion for selecting noise dominated pixels in the I_0 is set other than 1σ of the noise.

We thus apply the revised noise correction to A_0 . The details for updated definition of A_0 is given in Section 3.1. In contrast to the Petrosian radius, the size of a galaxy is directly determined by the segmentation map when A_0 is computed. We find that

our new method for noise correction is reliable when A or A_0 of a galaxy is measured and thus is independent on the size of the galaxy.

REFERENCES

- Allen, P. D., Driver, S. P., Graham, A. W., et al. 2006, *MNRAS*, 371, 2
- Andrae, R., & Jahnke, K. 2011, *MNRAS*, 418, 2014
- Barden, M., Jahnke, K., Häußler, B. 2008, *ApJS*, 175, 105
- Barnes, J. E. 2016, *MNRAS*, 455, 1957
- Barnes, J. E. 1992, *ApJ*, 393, 484
- Barton, E. J., Arnold, J. A., Zentner, A. R., Bullock, J. S., & Wechsler, R. H. 2007, *ApJ*, 671, 1538
- Bell, E. F., & de Jong, R. S. 2001, *ApJ*, 550, 212
- Bell, E. F., McIntosh, D. H., Katz, N., & Weinberg, M. D. 2003, *ApJS*, 149, 289
- Bell, E. F., Naab, T., McIntosh, D. H., et al. 2006, *ApJ*, 640, 241
- Bell, E. F., Wolf, C., Meisenheimer, K., et al. 2004, *ApJ*, 608, 752
- Bell, E. F., Zheng, X. Z., Papovich, C., et al. 2007, *ApJ*, 663, 834
- Bertin, E., & Arnouts, S. 1996, *A&AS*, 117, 393
- Bluck, A. F. L., Conselice, C. J., Bouwens, R. J., et al. 2009, *MNRAS*, 394, L51
- Bluck, A. F. L., Conselice, C. J., Buitrago, F., et al. 2012, *ApJ*, 747, 34
- Bois, M., Emsellem, E., Bournaud, F., et al. 2011, *MNRAS*, 416, 1654
- Bond, J. R., Kofman, L., & Pogosyan, D. 1996, *Nature*, 380, 603
- Borch, A., Meisenheimer, K., Bell, E. F., et al. 2006, *A&A*, 453, 869
- Bournaud, F., & Duc, P.-A. 2006, *A&A*, 456, 481
- Bournaud, F., Chapon, D., Teyssier, R., et al. 2011, *ApJ*, 730, 4
- Bournaud, F. 2010, *Advances in Astronomy*, 2010, 735284
- Braine, J., Duc, P.-A., Lisenfeld, U., et al. 2001, *A&A*, 378, 51
- Brammer, G. B., van Dokkum, P. G., & Coppi, P. 2008, *ApJ*, 686, 1503
- Brennan, R., Pandya, V., Somerville, R. S., et al. 2015, *MNRAS*, 451, 2933
- Bridge, C. R., Carlberg, R. G., & Sullivan, M. 2010, *ApJ*, 709, 1067 (B10)
- Buitrago, F., Trujillo, I., Conselice, C. J., Häußler, B. 2013, *MNRAS*, 428, 1460
- Bundy, K., Ellis, R. S., & Conselice, C. J. 2005, *ApJ*, 625, 621
- Bundy, K., Fukugita, M., Ellis, R. S., et al. 2009, *ApJ*, 697, 1369
- Caldwell, J. A. R., McIntosh, D. H., Rix, H.-W., et al. 2008, *ApJS*, 174, 136
- Cervantes-Sodi, B., Hernandez, X., & Park, C. 2010, *MNRAS*, 402, 1807
- Conn, B. C., Pasquali, A., Pompei, E., et al. 2011, *ApJ*, 741, 80
- Conselice, C. J. 2014, *ARA&A*, 52, 291
- Conselice, C. J. 2006, *ApJ*, 638, 686
- Conselice, C. J. 2003, *ApJS*, 147, 1
- Conselice, C. J., Rajgor, S., & Myers, R. 2008, *MNRAS*, 386, 909
- Conselice, C. J., Yang, C., & Bluck, A. F. L. 2009, *MNRAS*, 394, 1956
- Cowie, L. L., Songaila, A., Hu, E. M., & Cohen, J. G. 1996, *AJ*, 112, 839
- Croton, D. J., Springel, V., White, S. D. M., et al. 2006, *MNRAS*, 365, 11
- Davis, M., Guhathakurta, P., Konidaris, N. P., et al. 2007, *ApJ*, 660, L1
- de Jong, R. S. 1996, *A&A*, 313, 377
- de Ravel, L., Le Fèvre, O., Tresse, L., et al. 2009, *A&A*, 498, 379
- Dekel, A., & Burkert, A. 2014, *MNRAS*, 438, 1870
- Dekel, A., Sari, R., & Ceverino, D. 2009, *ApJ*, 703, 785
- Di Matteo, T., Springel, V., & Hernquist, L. 2005, *Nature*, 433, 604
- Driver, S. P., Liske, J., Cross, N. J. G., De Propriis, R., & Allen, P. D. 2005, *MNRAS*, 360, 81
- Duc, P.-A., Bournaud, F., & Masset, F. 2004, *A&A*, 427, 803
- Duc, P.-A., & Renaud, F. 2013, *Lecture Notes in Physics*, Berlin Springer Verlag, 861, 327
- Elmegreen, B. G., Elmegreen, D. M., Fernandez, M. X., & Lemonias, J. J. 2009, *ApJ*, 692, 12
- Elmegreen, D. M., Elmegreen, B. G., Ferguson, T., & Mullan, B. 2007a, *ApJ*, 663, 734
- Elmegreen, D. M., Elmegreen, B. G., & Hirst, A. C. 2004, *ApJ*, 604, L21
- Elmegreen, D. M., Elmegreen, B. G., Ravindranath, S., & Coe, D. A. 2007b, *ApJ*, 658, 763
- Förster Schreiber, N. M., Genzel, R., Bouché, N., et al. 2009, *ApJ*, 706, 1364
- Förster Schreiber, N. M., Shapley, A. E., Erb, D. K., et al. 2011, *ApJ*, 731, 65
- Faber, S. M., Willmer, C. N. A., Wolf, C., et al. 2007, *ApJ*, 665, 265
- Fakhouri, O., & Ma, C.-P. 2008, *MNRAS*, 386, 577
- Fakhouri, O., Ma, C.-P., & Boylan-Kolchin, M. 2010, *MNRAS*, 406, 2267
- Ferreras, I., Trujillo, I., Marmol-Queralto, E., et al. 2014, *MNRAS*, 444, 906
- Fiacconi, D., Mapelli, M., Ripamonti, E., & Colpi, M. 2012, *MNRAS*, 425, 2255
- Fogarty, L., Thatte, N., Tecza, M., et al. 2011, *MNRAS*, 417, 835
- Gavazzi, G., Pierini, D., & Boselli, A. 1996, *A&A*, 312, 397
- Genel, S., Genzel, R., Bouché, N., Naab, T., & Sternberg, A. 2009, *ApJ*, 701, 2002
- Giavalisco, M., Ferguson, H. C., Koekemoer, A. M., et al. 2004, *ApJ*, 600, L93
- Gladders, M. D., & Yee, H. K. C. 2005, *ApJS*, 157, 1
- Gottlöber, S., Klypin, A., & Kravtsov, A. V. 2001, *ApJ*, 546, 223
- Guo, K., Zheng, X. Z., Wang, T., & Fu, H. 2015, *ApJ*, 808, L49
- Hogg, D. W. 1999, *arXiv:astro-ph/9905116*
- Hopkins, P. F., Cox, T. J., Kereš, D., & Hernquist, L. 2008, *ApJS*, 175, 390
- Hopkins, P. F., Croton, D., Bundy, K., et al. 2010, *ApJ*, 724, 915
- Hopkins, P. F., Hernquist, L., Cox, T. J., et al. 2006, *ApJS*, 163, 1
- Howard, S., Keel, W. C., Byrd, G., & Burke, J. 1993, *ApJ*, 417, 502
- Hoyos, C., Aragón-Salamanca, A., Gray, M. E., et al. 2012, *MNRAS*, 419, 2703
- Ilbert, O., McCracken, H. J., Le Fèvre, O., et al. 2013, *A&A*, 556, A55
- Immeli, A., Samland, M., Gerhard, O., & Westera, P. 2004a, *A&A*, 413, 547
- Immeli, A., Samland, M., Westera, P., & Gerhard, O. 2004b, *ApJ*, 611, 20
- Ji, I., Peirani, S., & Yi, S. K. 2014, *A&A*, 566, A97
- Jogee, S., Miller, S. H., Penner, K., et al. 2009, *ApJ*, 697, 1971
- Karim, A., Schinnerer, E., Martínez-Sansigre, A., et al. 2011, *ApJ*, 730, 61
- Kartaltepe, J. S., Sanders, D. B., Scoville, N. Z., et al. 2007, *ApJS*, 172, 320
- Kauffmann, G., White, S. D. M., & Guiderdoni, B. 1993, *MNRAS*, 264, 201
- Keenan, R. C., Foucaud, S., De Propriis, R., et al. 2014, *ApJ*, 795, 157
- Kirby, E. M., Jerjen, H., Ryder, S. D., & Driver, S. P. 2008, *AJ*, 136, 1866
- Kitzbichler, M. G., & White, S. D. M. 2008, *MNRAS*, 391, 1489
- Koekemoer, A. M., Aussel, H., Calzetti, D., et al. 2007, *ApJS*, 172, 196
- Kriek, M., van Dokkum, P. G., Labbé, I., et al. 2009, *ApJ*, 700, 221
- López-Sanjuan, C., Balcells, M., Pérez-González, P. G., et al. 2009, *A&A*, 501, 505
- López-Sanjuan, C., Cenarro, A. J., Varela, J., et al. 2015, *A&A*, 576, A53
- López-Sanjuan, C., Le Fèvre, O., Ilbert, O., et al. 2012, *A&A*, 548, A7
- Lackner, C. N., Silverman, J. D., Salvato, M., et al. 2014, *AJ*, 148, 137
- Lawrence, A., Warren, S. J., Almaini, O., et al. 2007, *MNRAS*, 379, 1599
- Leauthaud, A., Massey, R., Kneib, J.-P., et al. 2007, *ApJS*, 172, 219
- Lee, J., & Pen, U.-L. 2002, *ApJ*, 567, L111
- Lee, J. 2011, *ApJ*, 732, 99
- Lilly, S. J., Le Fèvre, O., Hammer, F., & Crampton, D. 1996, *ApJ*, 460, L1
- Lilly, S. J., Le Brun, V., Maier, C., et al. 2009, *ApJS*, 184, 218
- Lin, L., Koo, D. C., Willmer, C. N. A., et al. 2004, *ApJ*, 617, L9
- Lin, L., Patton, D. R., Koo, D. C., et al. 2008, *ApJ*, 681, 232
- Liske, J., Lemon, D. J., Driver, S. P., Cross, N. J. G., & Couch, W. J. 2003, *MNRAS*, 344, 307
- Lisker, T. 2008, *ApJS*, 179, 319
- Lotz, J. M., Davis, M., Faber, S. M., et al. 2008b, *ApJ*, 672, 177
- Lotz, J. M., Jonsson, P., Cox, T. J., et al. 2011, *ApJ*, 742, 103
- Lotz, J. M., Jonsson, P., Cox, T. J., & Primack, J. R. 2010a, *MNRAS*, 404, 575
- Lotz, J. M., Jonsson, P., Cox, T. J., & Primack, J. R. 2010b, *MNRAS*, 404, 590
- Lotz, J. M., Jonsson, P., Cox, T. J., & Primack, J. R. 2008a, *MNRAS*, 391, 1137
- Lotz, J. M., Primack, J., & Madau, P. 2004, *AJ*, 128, 163
- Madau, P., Ferguson, H. C., Dickinson, M. E., et al. 1996, *MNRAS*, 283, 1388
- Madau, P., & Dickinson, M. 2014, *ARA&A*, 52, 415
- Man, A. W. S., Toft, S., Zirm, A. W., Wuyts, S., & van der Wel, A. 2012, *ApJ*, 744, 85
- Mapelli, M., & Mayer, L. 2012, *MNRAS*, 420, 1158
- McCracken, H. J., Milvang-Jensen, B., Dunlop, J., et al. 2012, *A&A*, 544, A156
- Mihos, J. C., & Hernquist, L. 1996, *ApJ*, 464, 641
- Milvang-Jensen, B., Freudling, W., Zabl, J., et al. 2013, *A&A*, 560, A94
- Mortlock, A., Conselice, C. J., Bluck, A. F. L., et al. 2011, *MNRAS*, 413, 2845
- Moustakas, J., Coil, A. L., Aird, J., et al. 2013, *ApJ*, 767, 50
- Muzzin, A., Marchesini, D., Stefanon, M., et al. 2013, *ApJS*, 206, 8
- Newman, A. B., Ellis, R. S., Bundy, K., & Treu, T. 2012, *ApJ*, 746, 162
- Owensworth, J. R., Conselice, C. J., Mortlock, A., et al. 2014, *MNRAS*, 445, 2198
- Petrosian, V. 1976, *ApJ*, 209, L1
- Rix, H.-W., Barden, M., Beckwith, S. V. W., et al. 2004, *ApJS*, 152, 163
- Rodriguez-Gomez, V., Genel, S., Vogelsberger, M., et al. 2015, *MNRAS*, 449, 49
- Schäfer, B. M. 2009, *International Journal of Modern Physics D*, 18, 173
- Schreiber, C., Pannella, M., Elbaz, D., et al. 2015, *A&A*, 575, A74
- Scoville, N., Aussel, H., Brusa, M., et al. 2007, *ApJS*, 172, 1
- Shandarin, S. F., & Zeldovich, Y. B. 1989, *Reviews of Modern Physics*, 61, 185
- Shapley, A. E. 2011, *ARA&A*, 49, 525
- Shi, Y., Rieke, G., Lotz, J., & Perez-Gonzalez, P. G. 2009, *ApJ*, 697, 1764
- Skrutskie, M. F., Cutri, R. M., Stiening, R., et al. 2006, *AJ*, 131, 1163
- Slosar, A., Land, K., Bamford, S., et al. 2009, *MNRAS*, 392, 1225
- Somerville, R. S., Hopkins, P. F., Cox, T. J., Robertson, B. E., & Hernquist, L. 2008, *MNRAS*, 391, 481
- Speagle, J. S., Steinhardt, C. L., Capak, P. L., & Silverman, J. D. 2014, *ApJS*, 214, 15
- Springel, V., Di Matteo, T., & Hernquist, L. 2005a, *MNRAS*, 361, 776
- Springel, V., Di Matteo, T., & Hernquist, L. 2005b, *ApJ*, 620, L79
- Tempel, E., Stoica, R. S., & Saar, E. 2013, *MNRAS*, 428, 1827
- Tempel, E., & Libeskind, N. I. 2013, *ApJ*, 775, L42
- Tomczak, A. R., Quadri, R. F., Tran, K.-V. H., et al. 2014, *ApJ*, 783, 85
- Toomre, A., & Toomre, J. 1972, *ApJ*, 178, 623
- Trujillo, I., Carretero, C., & Patiri, S. G. 2006, *ApJ*, 640, L111

- van der Wel, A., Franx, M., van Dokkum, P. G., et al. 2014, *ApJ*, 788, 28
- van Dokkum, P. G. 2005, *AJ*, 130, 2647
- Varela, J., Betancort-Rijo, J., Trujillo, I., & Ricciardelli, E. 2012, *ApJ*, 744, 82
- Vulcani, B., Marchesini, D., De Lucia, G., et al. 2016, *ApJ*, 816, 86
- Weilbacher, P. M., Duc, P.-A., & Fritze-v. Alvensleben, U. 2003, *A&A*, 397, 545
- Wen, Z. Z., Zheng, X. Z., & An, F. X. 2014, *ApJ*, 787, 130
- Wen, Z.-Z., Zheng, X.-Z., Zhao, Y.-H., & Gao, Y. 2012, *Ap&SS*, 337, 729
- Wetzstein, M., Naab, T., & Burkert, A. 2007, *MNRAS*, 375, 805
- Whitaker, K. E., Franx, M., Bezanson, R., et al. 2015, *ApJ*, 811, L12
- White, S. D. M., & Rees, M. J. 1978, *MNRAS*, 183, 341
- Williams, R. J., Quadri, R. F., Franx, M., van Dokkum, P., & Labbé, I. 2009, *ApJ*, 691, 1879
- Williams, R. J., Quadri, R. F., & Franx, M. 2011, *ApJ*, 738, L25
- Wirth, G. D., Willmer, C. N. A., Amico, P., et al. 2004, *AJ*, 127, 3121
- Xu, C. K., Zhao, Y., Scoville, N., et al. 2012, *ApJ*, 747, 85
- Yang, X., van den Bosch, F. C., Mo, H. J., et al. 2006, *MNRAS*, 369, 1293
- Yee, H. K. C., Morris, S. L., Lin, H., et al. 2000, *ApJS*, 129, 475
- Zhang, Y., Yang, X., Faltenbacher, A., et al. 2009, *ApJ*, 706, 747
- Zhang, Y., Yang, X., Wang, H., et al. 2013, *ApJ*, 779, 160
- Zhang, Y., Yang, X., Wang, H., et al. 2015, *ApJ*, 798, 17
- Zheng, X. Z., Bell, E. F., Papovich, C., et al. 2007, *ApJ*, 661, L41